The most distant, luminous, dusty star-forming galaxies: redshifts from NOEMA and ALMA spectral scans

Y. Fudamoto, R. J. Ivison, I. Oteo, M. Krips, Z. -Y. Zhang, A. Weiss, H. Dannerbauer, A. Omont, S. C. Chapman, L. Christensen, et al.

Monthly Notices
of the
ROYAL ASTRONOMICAL SOCIETY

MNRAS **472,** 2028–2041 (2017)
Advance Access publication 2017 August 2

doi:10.1093/mnras/stx1956

The most distant, luminous, dusty star-forming galaxies: redshifts from NOEMA and ALMA spectral scans

Y. Fudamoto,[1,2★] R. J. Ivison,[2,3] I. Oteo,[3,2] M. Krips,[4] Z.-Y. Zhang,[3,2] A. Weiss,[5] H. Dannerbauer,[6,7] A. Omont,[8,9] S. C. Chapman,[10] L. Christensen,[11] V. Arumugam,[2,3] F. Bertoldi,[12] M. Bremer,[13] D. L. Clements,[14] L. Dunne,[3,15] S. A. Eales,[15] J. Greenslade,[14] S. Maddox,[3,15] P. Martinez-Navajas,[7] M. Michalowski,[3] I. Pérez-Fournon,[6,7] D. Riechers,[16] J. M. Simpson,[3,17] B. Stalder,[18] E. Valiante[15] and P. van der Werf[19]

Affiliations are listed at the end of the paper

Accepted 2017 July 27. Received 2017 July 26; in original form 2017 June 15

ABSTRACT

We present 1.3- and/or 3-mm continuum images and 3-mm spectral scans, obtained using Northern Extended Millimeter Array (NOEMA) and Atacama Large Millimeter Array (ALMA), of 21 distant, dusty, star-forming galaxies. Our sample is a subset of the galaxies selected by Ivison et al. on the basis of their extremely red far-infrared (far-IR) colours and low *Herschel* flux densities; most are thus expected to be unlensed, extraordinarily luminous starbursts at $z \gtrsim 4$, modulo the considerable cross-section to gravitational lensing implied by their redshift. We observed 17 of these galaxies with NOEMA and four with ALMA, scanning through the 3-mm atmospheric window. We have obtained secure redshifts for seven galaxies via detection of multiple CO lines, one of them a lensed system at $z = 6.027$ (two others are also found to be lensed); a single emission line was detected in another four galaxies, one of which has been shown elsewhere to lie at $z = 4.002$. Where we find no spectroscopic redshifts, the galaxies are generally less luminous by 0.3–0.4 dex, which goes some way to explaining our failure to detect line emission. We show that this sample contains the most luminous known star-forming galaxies. Due to their extreme star-formation activity, these galaxies will consume their molecular gas in $\lesssim 100$ Myr, despite their high molecular gas masses, and are therefore plausible progenitors of the massive, 'red-and-dead' elliptical galaxies at $z \approx 3$.

Key words: ISM: molecules – galaxies: high-redshift – galaxies: ISM – galaxies: starburst.

1 INTRODUCTION

It has been known since the 1970s and 1980s that a large fraction of the energy produced by vigorously star-forming galaxies in the nearby Universe is radiated by cool dust that mingles with their reservoirs of molecular gas (e.g. Soifer, Neugebauer & Houck 1987). A decade on, the existence of a more distant population of dusty galaxies was inferred by Puget et al. (1996) from the detection of the cosmic far-infrared (far-IR) background using FIRAS aboard the *Cosmic Background Explorer*, individual examples of which were quickly detected by Smail, Ivison & Blain (1997) in the submillimetre (submm) waveband. If their initial stellar mass function (IMF) is normal, these galaxies form stars at tremendous rates, sometimes (>)1000 $M_\odot$ yr^{-1} (e.g. Ivison et al. 1998). Deeper submm observations in cosmological deep fields (e.g. Barger et al. 1998; Hughes et al. 1998; Eales et al. 1999) confirmed the abundance of these so-called submm galaxies (SMGs), sometimes known now as dusty, star-forming galaxies (DSFGs – e.g. Casey, Narayanan & Cooray 2014).

In the decades since then, the SPIRE camera (Griffin et al. 2010) aboard *Herschel* (Pilbratt et al. 2010) and the Submillimetre Common-User Bolometer Array-2 (SCUBA-2) camera (Holland et al. 2013) on the James Clerk Maxwell Telescope (JCMT) have together detected orders of magnitude more of these DSFGs. Conventional optical and near-IR spectroscopic observations confirmed that DSFGs are considerably more abundant (≈1000 ×) at high redshift than in the local Universe, with a redshift distribution for those selected at 850 μm that peaks at $z \sim 1$–3 (e.g. Chapman et al. 2005; Simpson et al. 2014). Those selected at (>) 1 mm by the South Pole

★ E-mail: yoshinobu.fudamoto@unige.ch

Telescope (e.g. Vieira et al. 2010; Strandet et al. 2017) are more distant while those selected at the far-IR wavelengths imaged by *Herschel* are typically at $z < 2$.

In the local Universe, massive early-type galaxies have old stellar populations, (>) 2 Gyr, and are therefore red in optical colour – so-called 'red-and-dead' galaxies. They have little gas or dust, and star-formation activity has ceased (see Renzini 2006, for a review, cf. Eales et al. 2017). The majority of these galaxies experienced an intense phase of star formation around 5–10 Gyr ago (e.g. Thomas et al. 2010), and current observational evidence suggests that DSFGs at $z \approx 2$ are their likely progenitors.

It is also well established that there exists a population of massive elliptical galaxies at $z \sim 2$–3. It has been claimed that most of these are high-redshift analogues of local, massive red-and-dead galaxies (i.e. high stellar masses, red colours, old stellar populations – see e.g. Cimatti et al. 2004; Trujillo et al. 2006; Kriek et al. 2008; van Dokkum & Brammer 2010, see also Dunlop et al. 1996 for a rarer but similarly old galaxy at $z = 1.55$). The existence of these galaxies at $z \sim 2$–3 suggests intense star-formation episodes must occur at even higher redshifts, perhaps implying that DSFGs are common at $z \gtrsim 4$ (e.g. Toft et al. 2014).

Only a small number of DSFGs were known at $z \gtrsim 4$ until recently, most of them gravitationally lensed (e.g. Asboth et al. 2016). To address this issue, Ivison et al. (2016) recently exploited the widest available far-IR imaging survey, *H*-ATLAS (Eales et al. 2010), to create a sample of the faintest, reddest dusty galaxies, further improving their photometric redshifts via ground-based photometry from SCUBA-2 (Holland et al. 2013) and LABOCA (Siringo et al. 2009). The galaxies thus selected are expected to be largely unlensed,[1] luminous and very distant. Their vigorous star-formation activity thus tallies with the star-formation history required to build up the large mass of stars found in spheroidal galaxies at $z \approx 2$.

To confirm that the ultrared DSFGs selected by Ivison et al. do lie at $z \gtrsim 4$, which will strengthen their links with red-and-dead galaxies at $z \sim 2$–3, requires robust spectroscopic confirmation of their photometric redshifts. This is non-trivial when working in the traditional optical and near-IR regime, verging on impossible with current telescopes and instrumentation. Following the success of Cox et al. (2011), who scanned the 3-mm atmospheric window to determine the redshift of one of the brightest, reddest, lensed galaxies to emerge from *H*-ATLAS (see also Weiß et al. 2013), we have therefore obtained 3-mm spectral scans of 21 ultrared DSFGs from the Ivison et al. sample, as well as interferometric 0.85- and 1.3-mm imaging to better pinpoint their positions.

Our primary objective here is to determine robust spectroscopic redshifts for these DSFGs, via the detection of multiple molecular and/or atomic emission lines. Using these to fine-tune the far-IR/submm photometric techniques employed by Ivison et al. then allows us to more reliably determine the space density of DSFGs at $z \gtrsim 4$. In addition, we use our improved measurements of IR luminosity and our CO line luminosities to estimate physical properties, such as SFR and molecular gas mass. Finally, we compare these derived properties with those of other DSFGs at low and high redshifts, subject as usual to the considerable uncertainties imposed by $\alpha_{\rm CO}$ and the assumed IMF.

Where applicable, we assume a flat Universe with (Ω_m, Ω_Λ, h_0) = (0.3, 0.7, 0.7). In this cosmology, an arcsecond corresponds to 7.1 kpc at $z = 4$.

[1] Despite expecting a low lensing fraction, Ivison et al. and others have shown that strongly lensed galaxies are common at $z > 4$ due to the increase with redshift of the optical depth to lensing and the magnification bias; Oteo et al. (in preparation-a) present high-resolution ALMA imaging of this sample, showing that the fraction of lensed galaxies is indeed relatively high.

Table 1. Targets for which 3-mm spectral scans were obtained.

Nickname	IAU name[a]
SGP-196076[b] (SGP-38326[c])	HATLAS J000306.9−330248
SGP-261206[b]	HATLAS J000607.6−322639
SGP-354388[b, d]	HATLAS J004223.5−334340
SGP-32338[b]	HATLAS J010740.7−282711
G09-59393[e]	HATLAS J084113.6−004114
G09-81106[e]	HATLAS J084937.0+001455
G09-83808[e]	HATLAS J090045.4+004125
G09-62610[e]	HATLAS J090925.0+015542
G15-26675	HATLAS J144433.3+001639
G15-82684[e]	HATLAS J145012.7+014813
NGP-206987[e]	HATLAS J125440.7+264925
NGP-111912[e]	HATLAS J130823.9+254514
NGP-136156[e]	HATLAS J132627.5+335633
NGP-126191[e]	HATLAS J133217.4+343945
NGP-284357	HATLAS J133251.5+332339
NGP-190387[e]	HATLAS J133337.6+241541
NGP-113609[e]	HATLAS J133836.0+273247
NGP-252305[e]	HATLAS J133919.3+245056
NGP-63663[e]	HATLAS J134040.3+323709
NGP-246114[e]	HATLAS J134114.2+335934
NGP-101333[e]	HATLAS J134119.4+341346

[a] As listed in Ivison et al. (2016).
[b] Observed with ALMA at 3 mm.
[c] Old nomenclature used by Oteo et al. (2016).
[d] Also known as the Great Red Hope (Oteo et al., in preparation-b).
[e] Observed with NOEMA at 1.3 mm as well as at 3 mm (Section 3.3).

2 SAMPLE SELECTION

Our targets – see Table 1 – were chosen from the faint, 'ultrared' galaxy sample of Ivison et al. (2016), taking those best suited to the latitudes of the telescopes we employ, with photometric redshifts consistent with $z \gtrsim 4$. Here, we briefly summarize the selection method used, referring readers to Ivison et al. (2016) for more details.

The sample was selected from the SPIRE images used to construct *H*-ATLAS Data Release 1 (Valiante et al. 2016), employing an optimal extraction kernel to minimize the effects of source confusion, which is especially pernicious at 500 μm. The reddest galaxies were isolated based on their SPIRE colours, such that $S_{500}/S_{250} \geq 1.5$ and $S_{500}/S_{350} \geq 0.85$, where S_{250} is the flux density measured at 250 μm (see Fig. 1). The galaxies thus selected have a median $S_{500} \sim 50$ mJy, such that the majority are not expected to be lensed gravitationally (e.g. Negrello et al. 2010; Conley et al. 2011, but see Oteo et al., in preparation-a).

The reddest of these SPIRE-selected galaxies were then imaged with SCUBA-2 (Holland et al. 2013) on the 15-m JCMT and/or with LABOCA (Siringo et al. 2009) on the 12-m Atacama Pathfinder Telescope (APEX) so that better photometric redshifts could be determined. These data are also utilized here, in Section 4.1, to aid us in spatially localizing any line emission. Of the 109 objects thus targeted by Ivison et al., 17 galaxies were selected for further

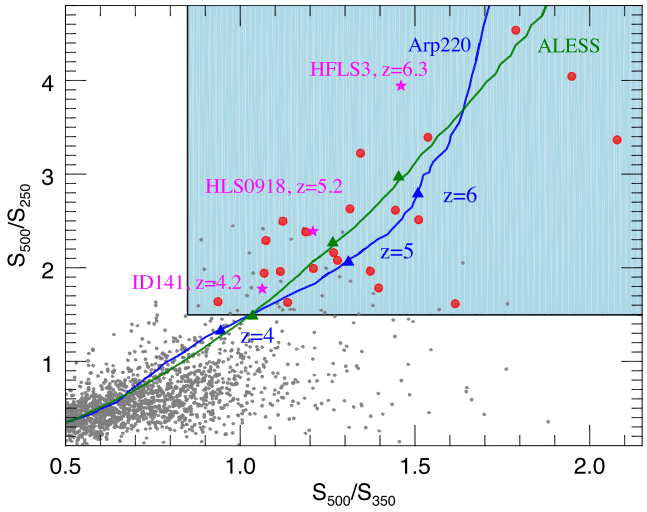

Figure 1. S_{500}/S_{350} versus S_{500}/S_{250} plot of our 21 targets (red circles), and SPIRE-selected DSFGs at $z > 4$ previously studied (magenta stars, Cox et al. 2011; Combes et al. 2012; Riechers et al. 2013). A sample of 1000 randomly selected *H*-ATLAS galaxies from Valiante et al. (2016) are shown as grey dots. We also show the redshift tracks of Arp 220 (blue line) and of a spectral energy distribution (SED) synthesized from 122 high-redshift DSFGs (green line; da Cunha et al. 2015) where triangles indicate $z = 4$, 5 and 6. Our targets satisfy the ultrared colour cuts, $S_{500}/S_{350} \geq 0.85$ and $S_{500}/S_{250} \geq 1.5$ (blue shaded area), expected for $z \gtrsim 4$ DSFGs (Ivison et al. 2016).

observations with the Institute Radioastronomie Millimetrique's (IRAM's) Northern Extended Millimeter Array (NOEMA) and four galaxies for further observations with the Atacama Large Millimeter Array (ALMA), based on their accessibility to those telescopes and their high photometric redshifts. The SPIRE flux densities and photometric redshifts determined by Ivison et al. (2016) are listed in Table 2.

3 OBSERVATIONS

3.1 NOEMA 3-mm spectral scans

Our observations with NOEMA[2] were conducted as two programmes (Program IDs: W05A, X0C6; Co-PIs: R. J. Ivison, M. Krips). Table 1 lists the galaxies observed. Both projects acquired data using five or six antennas in NOEMA's most compact (D) configuration. W05A was carried out between 2012 June and 2013 April, and 14 targets were observed. X0C6 took place between 2013 November and 2014 June, where four targets were observed. One target, G09-83808, was observed during both periods.

We employed multiple receiver tunings together with the WideX correlator – which provides 3.6 GHz of instantaneous dual-polarization bandwidth – to cover the 80–101.6-GHz part of the 3-mm atmospheric window, in which we expect to find at least one ^{12}CO transition for galaxies at $z > 3.6$ – see, for example, fig. 2 of Weiß et al. (2013), where for $3.6 < z < 7.5$ we always expect ^{12}CO(4–3), ^{12}CO(5–4) and/or ^{12}CO(6–5) in our frequency search range, with other lines such as C I(1–0) and H_2O(211–202) also present for some redshifts.

Different approaches were used during the two projects to maximize the probability of detecting multiple emission lines from each target, necessary to yield an unambiguous redshift (see discussion in Weiß et al. 2009). In W05A, once a single emission line was detected during an initial sweep of the 3-mm atmospheric window, the remaining 3-mm tunings were skipped and we instead tuned to a higher frequency, outside the 3-mm band, to search for a higher CO transition, having used the initial line and/or continuum detection to quantize the possibilities as well as to improve the photometric redshift estimate. In X0C6, spectra covering the 3-mm atmospheric window were obtained for all targets (∼21 GHz in total), then targets with emission lines were observed again to search for emission lines at higher frequencies, in the 2-mm band. Some of the targets therefore have less than 21 GHz of coverage (e.g. NGP-190387, NGP-126191 and G09-59393); others have coverage larger than 21 GHz (NGP-284357, NGP-246114 and G09-81106). Average on-source time per tuning was 20 min for W05A, and 120 min for X0C6, of which 15 and 90 min remained after flagging, respectively.

Calibration of the data was carried out by using the GILDAS package.[3] The typical resulting r.m.s. noise levels were 2.7 and 1.1 mJy beam^{-1} in 100-km s^{-1} channels for data taken in W05A and X0C6. Calibrated visibilities were converted into FITS format for export, then into MS format to be imaged by CASA (McMullin et al. 2007). The average synthesized beam size was 5 arcsec full width at half-maximum (FWHM) during both runs, with considerable diversity in beam shape due to the relatively short tracks.

To study any 3-mm continuum emission from our targets, we integrated our data over all observed frequencies, imaging with the CLEAN task in CASA, with a map size of 1 arcmin × 1 arcmin, sufficient to cover the 3-mm primary beam.

3.2 ALMA 3-mm spectral scans

Four ultrared galaxies were observed using ALMA (see Table 1), with five separate tunings to cover the 3-mm window (Program ID: 2013.1.00499.S; PI: A. Conley). Data were acquired during 2014 July 02–03 and August 28, with typically 8.6–9.7 min spent on-source for each tuning, in addition to 20 min of calibration – pointing, phase, flux density (Neptune) and bandpass.

Data were calibrated using the ALMA pipeline, with only minor flagging required. Calibrated data were imaged using CLEAN within CASA, using the natural weighting scheme to maximize sensitivity.

The resulting r.m.s. noise levels ranged between 0.73 and 0.80 mJy beam^{-1} in channels binned to 100 km s^{-1}. Because the observations were carried out on several different dates, with different antenna configurations, at frequencies ranging from 84 to 115 GHz, the resulting synthesized beamsizes varied between 0.6 and 1.2 arcsec FWHM.

As with our NOEMA data, 3-mm continuum images were created using all the available data, with a map size of 1 arcmin × 1 arcmin.

3.3 NOEMA 1.3-mm continuum observations

We have also carried out 1.3-mm observations of 10 galaxies lacking continuum detections, and hence accurate positions, in our earlier 3-mm work. Table 1 lists those targets observed during 2015 December (Program ID: W15ET; PI: M. Krips), again using the most compact NOEMA configuration, with six antennas. The typical resulting synthesized beam size was ∼1.5 arcsec FWHM. Calibration was accomplished following the standard procedures, using GILDAS,

[2] http://iram-institute.org/EN/noema-project.php

[3] http://www.iram.fr/IRAMFR/GILDAS

Table 2. Continuum flux-density measurements and redshifts, photometric and/or spectroscopic.

Nickname	S_{250}	S_{350}	S_{500}	S_{850}	$S^{a}_{1.3\ mm}$	$S^{a}_{3\ mm}$	z^{b}_{phot}	z_{spec}	Reference
SGP-196076	28.6 ± 7.3	28.6 ± 8.2	46.2 ± 8.6	32.5 ± 9.8	–	0.41 ± 0.03	$4.51^{+0.47}_{-0.39}$	4.425 ± 0.001	–
SGP-261206	22.6 ± 6.3	45.2 ± 8.0	59.4 ± 8.4	56.9 ± 8.9	–	0.38 ± 0.02	$5.03^{+0.58}_{-0.47}$	4.242 ± 0.001	–
SGP-354388	26.6 ± 8.0	39.8 ± 8.9	53.5 ± 9.8	39.9 ± 4.7	–	0.35 ± 0.02	$5.35^{+0.56}_{-0.52}$	4.002 ± 0.001	Oteo et al. (in preparation-b)
SGP-32338	16.0 ± 7.1	33.2 ± 8.0	63.7 ± 8.7	27.9 ± 9.4	–	0.21 ± 0.02	$3.93^{+0.26}_{-0.24}$	–	–
G09-59393	24.1 ± 7.0	43.8 ± 8.3	46.8 ± 8.6	27.7 ± 5.6	4.0 ± 0.6	–	$3.70^{+0.35}_{-0.26}$	–	–
G09-81106	14.0 ± 6.0	30.9 ± 8.2	47.5 ± 8.8	37.4 ± 11.4	9.7 ± 1.3	0.24 ± 0.04	$4.98^{+0.13}_{-0.73}$	4.531 ± 0.001	–
G09-83808	9.7 ± 5.4	24.6 ± 7.9	44.0 ± 8.2	36.2 ± 9.1	19.4 ± 2.0	0.66 ± 0.12	$5.66^{+0.06}_{-0.74}$	6.027 ± 0.001	Zavala et al. (2017)
G09-62610	18.6 ± 5.4	37.3 ± 7.4	44.3 ± 7.8	23.1 ± 9.0	5.2 ± 0.8	≤0.18	$3.70^{+0.44}_{-0.26}$	–	–
G15-26675	26.8 ± 6.3	57.2 ± 7.4	61.4 ± 7.7	36.6 ± 10.3	–	≤0.33	$4.36^{+0.25}_{-0.21}$	–	–
G15-82684	17.3 ± 6.4	38.5 ± 8.1	43.2 ± 8.8	15.3 ± 8.2	≤1.6	≤0.36	$3.65^{+0.38}_{-0.25}$	–	–
NGP-206987	24.1 ± 7.1	39.2 ± 8.2	50.1 ± 8.7	17.5 ± 6.5	9.2 ± 1.8	≤0.32	$4.07^{+0.06}_{-0.60}$	–	–
NGP-111912	25.2 ± 6.5	41.5 ± 7.6	50.2 ± 8.0	8.8 ± 6.7	4.7 ± 0.9	≤0.26	$3.27^{+0.36}_{-0.26}$	–	–
NGP-136156	29.3 ± 7.4	41.9 ± 8.3	57.5 ± 9.2	29.7 ± 4.6	3.1 ± 0.8	≤0.25	$3.95^{+0.06}_{-0.57}$	–	–
NGP-126191	24.5 ± 6.4	31.3 ± 7.7	43.7 ± 8.2	37.2 ± 7.5	12.3 ± 1.7	0.30 ± 0.11 [c]	$4.33^{+0.45}_{-0.46}$	–	–
NGP-284357	12.6 ± 5.3	20.4 ± 7.8	42.4 ± 8.3	27.4 ± 9.9	–	0.62 ± 0.03	$4.99^{+0.44}_{-0.45}$	4.894 ± 0.003	–
NGP-190387	25.2 ± 7.2	41.9 ± 8.0	63.3 ± 8.8	33.4 ± 8.0	12.2 ± 1.2	0.84 ± 0.14	$4.36^{+0.37}_{-0.26}$	4.420 ± 0.001	–
NGP-113609	29.4 ± 7.3	50.1 ± 8.0	63.5 ± 8.6	12.5 ± 6.2	13.0 ± 2.3	≤0.26	$3.43^{+0.34}_{-0.20}$	–	–
NGP-252305	15.3 ± 6.1	27.7 ± 8.1	40.0 ± 9.4	23.5 ± 7.6	6.5 ± 0.7	≤0.29	$4.34^{+0.43}_{-0.38}$	–	–
NGP-63663	30.6 ± 6.8	53.5 ± 7.8	50.1 ± 8.1	7.9 ± 8.3	≤1.3	≤0.24	$3.08^{+0.23}_{-0.22}$	–	–
NGP-246114	17.3 ± 6.5	30.4 ± 8.1	33.9 ± 8.5	32.4 ± 8.2	8.0 ± 1.5	0.42 ± 0.06	$4.35^{+0.53}_{-0.46}$	3.847 ± 0.002	–
NGP-101333	32.4 ± 7.5	46.5 ± 8.2	52.8 ± 9.0	17.6 ± 8.2	10.8 ± 1.3	≤0.25	$3.53^{+0.34}_{-0.27}$	–	–

[a]Measured flux density, or 3σ upper limit. Stated errors exceed the local r.m.s. in the relevant image, since they reflect all uncertainties, including source size.
[b]Photometric redshift estimated by template SED fits to 250-, 350-, 500- and 850- or 870-μm flux densities (Ivison et al. 2016).
[c]Tentative detection only.

with little need for significant flagging. The average time spent on-source was 25 min, yielding typical noise level of 0.47 mJy beam^{-1}.

We also use data from an earlier programme that observed another five of our targets – G09-81106, G09-83808, NGP-101333, NGP-126191 and NGP-246114 – taken during 2013 in the compact 6C configuration, with a typical resulting synthesized beam size of 1.0 arcsec × 1.3 arcsec FWHM, the major axis at a position angle of 25° (Program ID: W0BD; Co-PIs: F. Bertoldi, I. Perez-Fournon).

4 RESULTS

If detecting faint line emission from distant galaxies is challenging, doing so in the absence of an accurate position is considerably more so. For this reason, our first step is to explore the 3-mm continuum images described in Section 3, hoping that thermal dust emission from our luminous, dusty starbursts will betray the precise position of our targets.

4.1 Continuum emission

To determine the significance of any continuum emission, we measured the r.m.s. noise level of the maps, and then created the signal-to-noise ratio (SNR) images shown in Fig. 2.

All four sources observed at 3 mm with ALMA are clearly detected in continuum, at (>) 8σ significance.

For the objects observed at 3 mm with NOEMA, the sensitivity is much reduced compared to ALMA, so we begin by overlaying the 3-mm continuum images with contours from the deep SCUBA-2 850-μm imaging of Ivison et al. (2016), where the unsmoothed FWHM of the SCUBA-2 images is around 13 arcsec, and the r.m.s. pointing accuracy of the JCMT for a single visit to a target is ∼2–3 arcsec.

We then searched for faint 3-mm continuum sources coincident with SCUBA-2 850-μm emission, finding eight plausible sites. We discount the faint 3-mm emission seen towards G09-59393, favouring the 1.3-mm position a few arcseconds to the east, which is considerably more significant. The most dubious of the others is NGP-113609, although the close proximity of the 3-mm peak to the SCUBA-2 850-μm emission lends extra confidence. NGP-126191 displays ≥4σ emission; again, the near-coincidence with 850-μm and/or 1.3-mm emission gives additional confidence. For the five remaining sources, 3-mm continuum emission was detected at (>) 5σ.

Of the targets observed in continuum at 1.3 mm using NOEMA, we were able to measure positions and flux densities for 13 of 15.

The flux densities and coordinates of all these continuum detections are quoted in Tables 2 and 3, respectively, corrected for primary beam attenuation, including the small number of tentative examples (which are marked as such). The contribution from emission lines to the continuum flux density is negligible, as we shall see in what follows.

It is worth noting here that none of the ultrared galaxies observed in 1.3- or 3-mm continuum are revealed as doubles, as would be expected in the simulations of Bethermin et al. (2017), though it

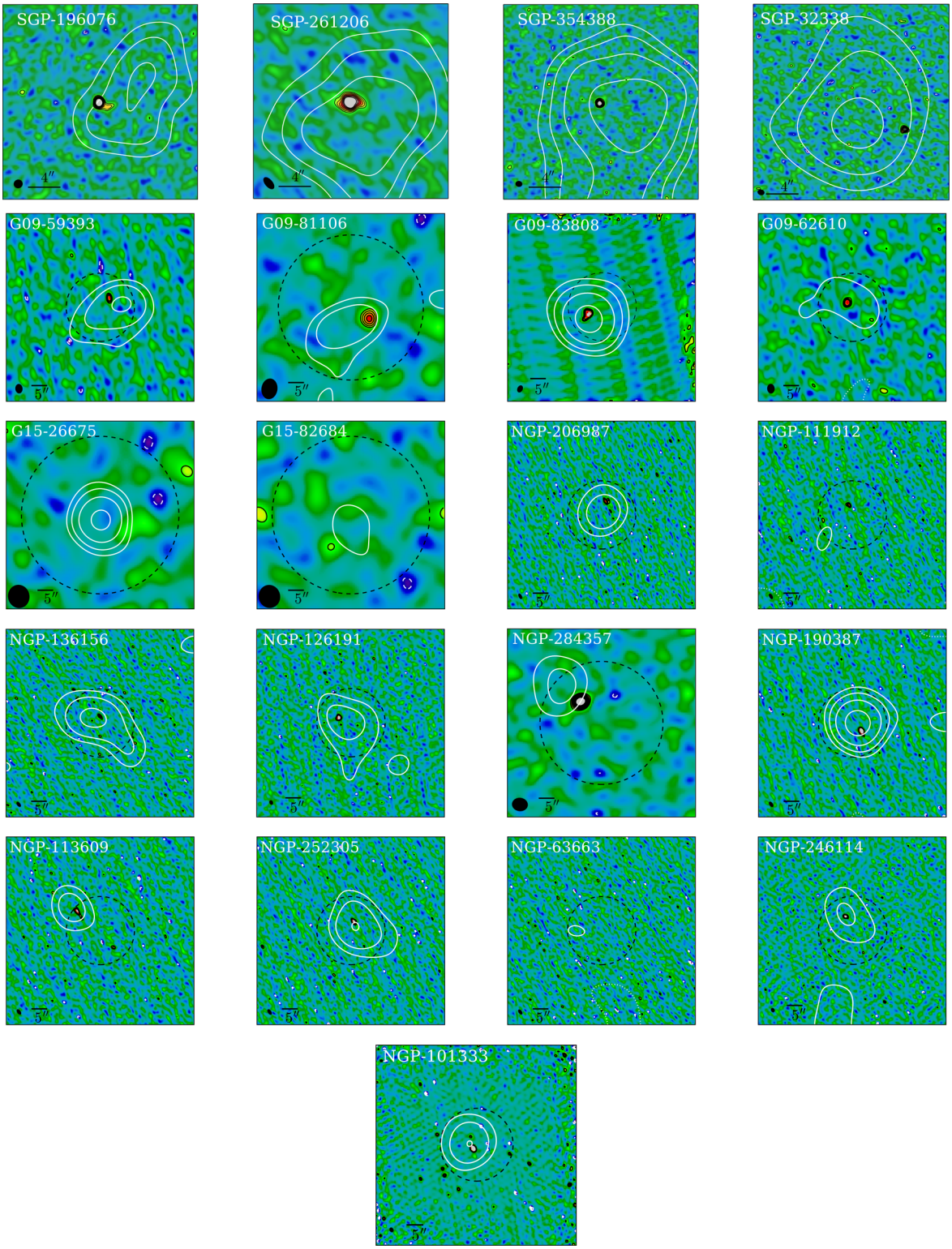

Figure 2. Continuum images of the 1.3- or 3-mm continuum data from ALMA *(top row)* and NOEMA, uncorrected for the primary beam response. Black contours represent the continuum emission, and start from 3σ. Black dashed lines indicate where the sensitivity (primary-beam response) drops to 50 per cent of the peak response (for ALMA at 3 mm, this region exceeds the size of the maps shown here). White contours represent 850-μm emission as detected by SCUBA-2, smoothed with a 13 arcsec Gaussian, with contours starting at 3σ and increasing in factors of $\sqrt{2}$, from Ivison et al. (2016). The SCUBA-2 images give an indication of where to expect 1.3- or 3-mm continuum emission. For the ten examples where 1.3- or 3-mm continuum is detected, we see typical offsets of ≈2–4 arcsec between the emission peaks detected by SCUBA-2 and the more precisely pinpointed 1.3- or 3-mm peaks detected by ALMA or NOEMA, consistent with the $\sigma = 2$–3 arcsec pointing accuracy of the JCMT for a single visit to a target, as was usually the case for the SCUBA-2 images shown here. Except for NGP-111912, all continuum detections are coincident with emission-line detections. White dashed contours indicate -3σ at 3 mm. Black ellipses indicate the synthesized beamsize. N is up; E is left.

Table 3. Precise J2000 positions of ultrared galaxies.

Nickname	RA	Dec.
SGP-196076[b] (aka SGP-38326)	00:03:07.22	−33:02:50.9
SGP-261206[b]	00:06:07.54	−32:26:39.9
SGP-354388[b] (aka GRH)	00:42:23.52	−33:43:23.5
SGP-32338[b]	01:07:41.00	−28:27:09.4
G09-59393[a]	08:41:13.42	−00:41:11.7
G09-81106[b]	08:49:36.82	+00:14:54.7
G09-83808[a, b]	09:00:45.79	+00:41:22.9
G09-62610[a]	09:09:25.18	+01:55:43.7
G15-26675	–	–
G15-82684	–	–
NGP-206987[a]	12:54:40.67	+26:49:29.6
NGP-111912[a]	13:08:24.04	+25:45:17.9
NGP-136156[a]	13:26:27.57	+33:56:35.5
NGP-126191[a]	13:32:17.76	+34:39:47.5
NGP-126191[d]	13:32:17.82	+34:39:50.5
NGP-284357[b]	13:32:51.73	+33:23:42.8
NGP-190387[a]	13:33:37.47	+24:15:39.3
NGP-113609[a, c]	13:38:36.65	+27:32:53.5
NGP-252305[a]	13:39:19.27	+24:50:59.4
NGP-63663	–	–
NGP-246114[a, b]	13:41:14.09	+33:59:38.2
NGP-101333[a]	13:41:19.36	+34:13:46.5

[a]Position determined via 1.3-mm continuum.
[b]Position determined via 3-mm continuum.
[c]Tentative continuum detection.
[d]Position determined via emission line.

Table 4. Measured properties of the detected emission lines.

Nickname	Transition	$\nu_{\rm line}$ (GHz)	Flux[a] (Jy km s^{-1})	FWHM[b] (km s^{-1})
SGP-196076[d]	CO(4–3)	84.97 ± 0.01	3.18 ± 0.34	1080 ± 90
	CO(5–4)	106.19 ± 0.02	1.22 ± 0.12	1280 ± 80
SGP-261206	CO(4–3)	87.95 ± 0.01	2.12 ± 0.33	440 ± 40
	CO(5–4)	109.01 ± 0.01	2.94 ± 0.33	440 ± 30
SGP-354388	C I(1–0)	98.39 ± 0.01	0.97 ± 0.22	700 ± 180
SGP-32338	CO(5–4)[c]	100.07 ± 0.01	1.70 ± 0.20	630 ± 80
G09-81106	CO(4–3)	83.36 ± 0.01	1.27 ± 0.21	570 ± 130
	CO(5–4)	104.19 ± 0.01	1.56 ± 0.33	470 ± 100
G09-83808	CO(5–4)	82.02 ± 0.02	0.92 ± 0.30	240 ± 100
	CO(6–5)	98.39 ± 0.01	0.87 ± 0.24	360 ± 110
NGP-111912	CO(4–3)[c]	95.15 ± 0.04	2.04 ± 0.79	440 ± 200
NGP-126191	CO(5–4)[c]	85.77 ± 0.02	3.19 ± 0.88	570 ± 180
NGP-284357	CO(6–5)	97.75 ± 0.03	2.37 ± 0.52	680 ± 180
	CO(7–6)	136.90 ± 0.09	2.70 ± 0.68	420 ± 150
NGP-190387	CO(4–3)	85.10 ± 0.02	2.52 ± 0.67	670 ± 250
	CO(5–4)	106.23 ± 0.02	2.69 ± 0.71	440 ± 150
NGP-246114	CO(4–3)	95.08 ± 0.02	1.36 ± 0.19	550 ± 150
	CO(6–5)	142.71 ± 0.03	1.60 ± 0.32	660 ± 140

[a]Measured via 2D Gaussian fit to zeroth moment image, after continuum subtraction.
[b]FWHM calculated via Gaussian fit to spectrum with 100-km s^{-1} spectral resolution.
[c]Most probable CO transition, based on the photometric redshift estimate from Ivison et al. (2016).
[d]Properties measured by combining all components.

remains possible that some or all of the ∼20 per cent of targets that remain undetected in continuum have been pushed below our interferometric detection threshold by multiplicity.

4.2 Searching for emission lines

To determine reliable, unambiguous redshifts for a DSFG, we must detect two or more emission lines. Ideally we must extract their spectra at known positions, typically betrayed by interferometric continuum detection in the cases of DSFGs, thereby maximizing the significance of any line detections. If we extract spectra blindly, we must correct our statistics for the number of independent sightlines explored. Here, our known positions come from the 1.3- and 3-mm continuum imaging with NOEMA and ALMA, as described in Section 4.1; for the 17 sources with reliable coordinates (Table 3), we extracted spectra at the precise positions of the corresponding continuum detections.

In the three cases where we have no continuum detection at either 1.3 or 3 mm, tagged as such in Table 3, we searched blindly for emission lines in data cubes that had not been corrected for the primary beam response. We convolved these data cubes along their frequency axis with box-car kernels of width 3, 4 and 7 channels, corresponding to velocity widths of ≈200–500 km s^{-1}, typical for DSFG emission lines (Bothwell et al. 2013). For each convolved cube we created an SNR cube, then searched for peaks above 5σ, where the significance of detections at this stage has not been corrected for the number of independent sightlines we have explored. We also performed the same blind line-search procedure on continuum-detected sources to look for any additional line emission. Only known lines were recovered.

As a result of these emission-line searches, we detected multiple (two or more) emission lines from seven of our targets, one of these following the detection of three lines by Zavala et al. (2017), as well as single emission lines from four targets, where more lines have been detected subsequently in one case (Oteo et al., in preparation-b). We thus report the first eight robust, accurate, unambiguous redshifts for faint, largely unlensed and thus intrinsically very luminous starbursts.

For all the detected emission lines, we have fitted single-component Gaussians, measuring the frequency of the line centre, and its FWHM. Continuum emission was subtracted with the UVCONTSUB task in CASA, using all available channels except those close to emission lines. The flux of each emission line has been measured with the CASA IMFIT task, from the zeroth moment map (created by integrating along the frequency axis across the emission line). There are no significant discrepancies between these values and those found from the Gaussian fits. The measured properties of the emission lines are summarized in Table 4.

4.3 Unambiguous redshifts via detection of multiple emission lines

We detect multiple emission lines towards seven of our targets, such that the redshifts of these sources and species/transitions of the emission lines are confirmed unambiguously. The properties of those sources are discussed in Section 6.

For NGP-190387, two emission lines are detected at 85.10 and at 106.23 GHz (see Fig. 3), CO(4–3) and CO(5–4) at $z = 4.420$ ($z = 4.418$ and 4.425, respectively, for the two lines). NGP-190387 lies close to a group of three faint ($K_{\rm AB} \approx 21$–22) galaxies, likely at $z \gtrsim 1$, revealed by NIRI on the 8-m Gemini North telescope (Fig. 4), which amplify the DSFG gravitationally by a factor we cannot constrain meaningfully at the present time.

Towards G09-81106 we have detected two emission lines, CO(4–3) and CO(5–4), at 83.36 and 104.19 GHz (Fig. 3), both at $z = 4.531$. There is no suggestion of gravitational lensing for G09-81106, either

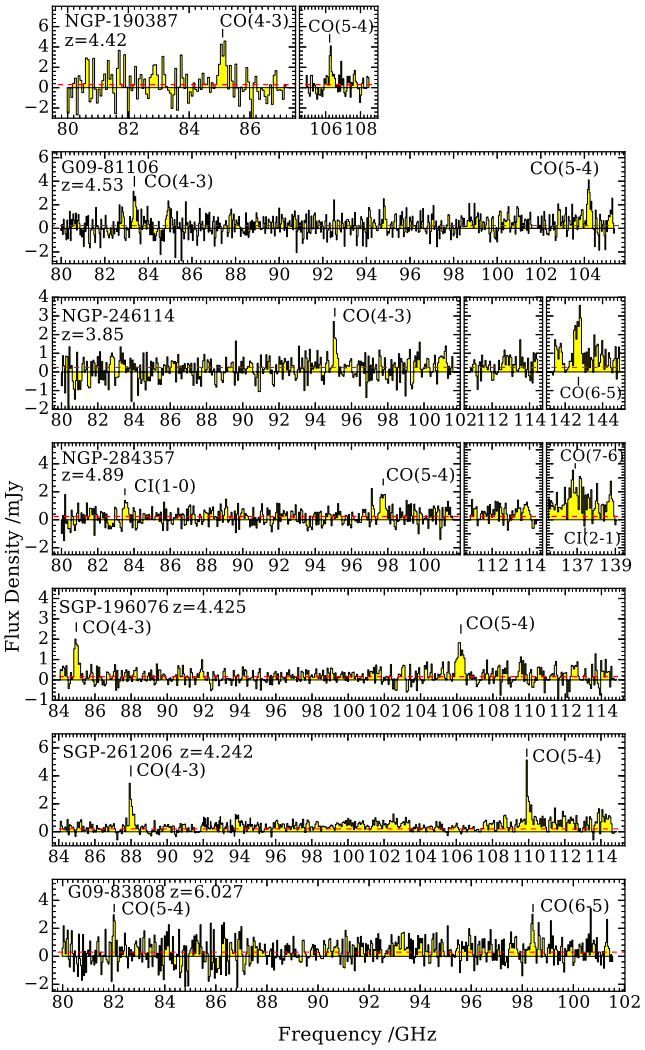

Figure 3. 3-mm spectra of targets with clear multiple line detections, thus yielding unambiguous redshifts, extracted at the positions where 3-mm continuum is seen. The spectra have been binned to 250, 150, 150, 200, 100, 100 and 100 km s^{-1}, from top to bottom, respectively. Red dashed lines show the median continuum flux density value calculated across the full frequency range, excluding ±0.5 GHz around the emission lines. All but two of the spectroscopic redshifts agree well with the photometric estimates of Ivison et al. (2016) – see Table 7. NGP-284357 shows C I(1–0) emission at the expected position, 83.6 GHz; however the line falls between WideX tunings, meaning the line properties are difficult to measure. C I(2–1) is located at ∼137.41, blended alongside ^{12}CO(7–6). Like many DSFGs, SGP-196076 comprises merging galaxies (Oteo et al. 2016), and here we show the combined spectrum of the two most luminous components.

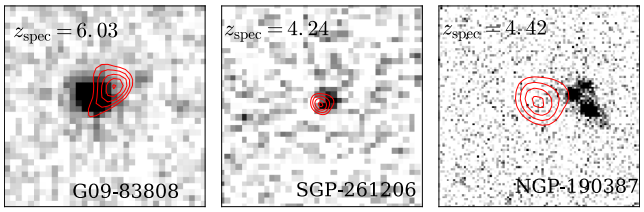

Figure 4. Near-IR (*K*-band) 11 arcsec × 11 arcsec images of G09-83808 and SGP-261206 from VIKING survey (Edge et al. 2013) and NGP-190387 from Gemini/NIRI (programme GN-2016A-FT-32). Red contours represent the 1.3-mm (G09-83808, NGP-190387) and 3-mm (SGP-261206) continuum emission, at 5, 6, 7, 8, 9 × σ. Near-IR emission is seen clearly, coincident or near-coincident with the 1.3- or 3-mm continuum emission. At the depth of the VIKING observations (limiting magnitude, $K_{AB} \simeq 21.2$), we do not expect to detect dust-obscured distant galaxies. The sources coincident with G09-83808 and SGP-261206 show, therefore, that these two DSFGs are amplified gravitationally by the foreground galaxies seen in the near-IR images. The galaxy in the foreground of SGP-83808 has $z_{spec} = 0.778$, obtained using X-shooter on the VLT (Fig. 5), and is magnified by 8.2 ± 0.3, a factor determined using high-resolution ALMA continuum imaging (see Oteo et al., in preparation-a). The three galaxies revealed by the deeper Gemini imaging of NGP-190387 are considerably fainter, with $K_{AB} = 21.0$, 22.3, 21.4, yet they are not coincident with the $z = 4.42$ DSFG and likely constitute a foreground lensing group.

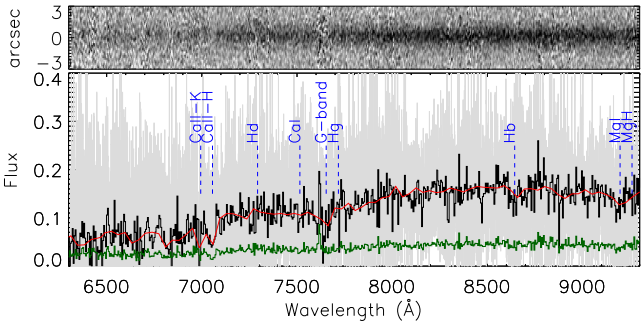

Figure 5. *Top:* Spectrum of the lensing galaxy in the foreground of SGP-83808, as seen in the optical arm of VLT/X-shooter after integrating for 4 × 20 min on 2013 March 17. *Below:* The 1D spectrum, in grey, extracted using a simple box-car summation [090.A-0891(A), PI: Christensen]. To identify the lens redshift we binned these data heavily (see Modigliani et al. 2010; Christensen et al. 2012; Kausch et al. 2014), as illustrated in black, with the error spectrum shown in green, then fitted the redshift by χ^2 minimization using a 5-Gyr stellar population model (shown in red) from Bruzual & Charlot (2003). We find $z_{spec} = 0.778 \pm 0.006$. Strong absorption features are labelled. The flux units are 10^{-17} erg s^{-1} cm^{-2} Å^{-1}.

via the presence of unusually bright near-IR galaxies in the field, or via its submm morphology as seen in high-resolution ALMA continuum imaging (Oteo et al., in preparation-a).

Towards G09-83808 we have detected two faint emission lines, at 82.02 and 98.39 GHz (Fig. 3), corresponding to CO(5–4) and CO(6–5) at $z = 6.026 \pm 0.001$ and 6.028 ± 0.001, respectively, so an average of 6.027 ± 0.001. These lines were also noted by Zavala et al. (2017) in a spectrum obtained using the Large Millimeter Telescope. G09-83808 is near-coincident with a foreground galaxy, seen clearly in near-IR imaging from the VIKING survey (see Fig. 4 – Edge et al. 2013), indicative of gravitationally lensing. This foreground galaxy has a spectroscopic redshift of 0.778, obtained using X-shooter on the 8-m Very Large Telescope (VLT; see Fig. 5). A lens model based on the morphology determined by high-resolution ALMA continuum imaging predicts a gravitational amplification of 8.2 ± 0.3 (Oteo et al., in preparation-a).

For NGP-284357, we find at least two emission lines, at 97.75 and 136.9 GHz (Fig. 3). If these are CO(5–4) and CO(7–6), the redshifts are 4.895 and 4.892, respectively, so an average of $z = 4.894$. At this redshift, the fine-structure lines of neutral carbon are expected at 83.54 and 137.41 GHz, respectively, and we see strong hints of corresponding emission – a discrete feature where C I(1–0) is expected, and C I(2–1) appears to be broadening the CO(7–6) line.

In the case of NGP-246114, two emission lines are detected at 95.08 and 142.71 GHz (Fig. 3), which must be CO(4–3) and CO(6–5) at $z = 3.849$ and 3.845, respectively, so an average of $z = 3.847$.

Table 5. Line luminosity ratios of CO lines.

Object	CO transitions	Line luminosity ratio	Bothwell[a]
SGP-196076	5–4/4–3	0.81 ± 0.15	0.78 ± 0.18
SGP-261206	5–4/4–3	0.90 ± 0.17	0.78 ± 0.18
G09-81106	5–4/4–3	0.80 ± 0.21	0.78 ± 0.18
G09-83808	6–5/5–4	0.66 ± 0.28	0.66 ± 0.16
NGP-284357	7–6/5–4	0.58 ± 0.19	0.56 ± 0.15
NGP-190387	5–4/4–3	0.69 ± 0.26	0.78 ± 0.18
NGP-246114	6–5/4–3	0.52 ± 0.13	0.51 ± 0.13

[a] Average line luminosity ratio for SMGs from Bothwell et al. (2013).

SGP-196076 has been studied in detail by Oteo et al. (2016), who referred to the galaxy as SGP-38326, an *H*-ATLAS **nomenclature pre-dating Ivison et al. (2016); for further details we refer the readers to that paper. Summarizing the main results obtained from our 3-mm spectral scans of SGP-196076: we have detected the CO(5–4) and CO(4–3) transitions at 84.97 and 106.19 GHz, so at $z = 4.425$ (Fig. 3). C I is also seen, at low significance. Both the continuum emission, from dust, and the CO(5–4) line emission, indicate clearly that SGP-196076 comprises multiple (≥3) components, with the star formation in each one presumably triggered by their close proximity – an ongoing merger or strong interaction. Oteo et al. (2016) explored the velocity field of the two largest components, via their CO and [C II] emission, finding ordered disc-like rotation.

SGP-261206 displays emission lines at 87.95 and 109.01 GHz (Fig. 3), CO(4–3) and CO(5–4) at $z = 4.242 \pm 0.001$, around 1.7σ below its photometric redshift. C I is also seen, at low significance. Very dust-obscured, distant galaxies should not be coincident with near-IR sources at the depth of our available imaging, unless those near-IR sources are gravitationally lensing the dusty galaxy. However, the *K*-band image[4] of SGP-261206 shown in Fig. 4, from VIKING (Edge et al. 2013), contains a clear *K*-band counterpart, coincident with the dust emission. This suggests that SGP-261206 is gravitationally lensed by the foreground galaxy detected in the near-IR image, a hint confirmed by high-resolution ALMA imaging (Oteo et al., in preparation-a).

4.3.1 CO line ratios

Our spectra allow us to determine line luminosity ratios for those galaxies for which multiple lines were detected, typically anchored to ^{12}CO $J = 5$–4.

In Table 5 we list the CO line luminosity ratios (i.e. $L'_{\rm CO(i\,-\,i\text{-}1)}/L'_{\rm CO(j\,-\,j\text{-}1)}$) which we find are consistent with the average values found for SMGs by Bothwell et al. (2013).

4.3.2 Rest-frame stacking

For the eight spectra for which we have accurate, unambiguous redshifts, we can shift the data to the corresponding rest-frame frequencies and stack them to search for features fainter than the relatively bright ^{12}CO lines, following Spilker et al. (2015) and Zhang et al. (2017). The resulting stacked spectrum is shown in Fig. 6 where we find the expected ^{12}CO ladder between $J = 4$–3 and $J = 7$–6, the latter broadened by C I(2–1), as well as weak C I(1–0) line emission. Absorption due to the collisionally excited H_2O $1_{1,\,0}$–$1_{0,\,1}$ ground transition[5] may be seen, at low ($\approx 2.5\sigma$) significance.

4.3.3 Detection of single emission lines

Towards four of our galaxies, single emission lines were detected, insufficient to determine the redshift of the source unambiguously, as the species and/or transition of the emission line is unknown. However, combining the redshift constraint available by virtue of far-IR/submm colour, often only a handful of strong emission lines become plausible candidates.

Towards NGP-126191 we detected a clear emission line at 85.77 GHz (Fig. 7), with an FWHM of 570 ± 180 km s^{-1}. As outlined earlier, this line emission is ≈3 arcsec from weak 3-mm continuum emission, which may be spurious, or may be from a companion, or the dust emission may be slightly displaced from the line emission – a relatively common finding amongst DSFGs (e.g. Ivison et al. 2010a; Fu et al. 2013; Dye et al. 2015; Spilker et al. 2015; Oteo et al. 2016). With a far-IR/submm photometric redshift of 4.9, the most likely identification for this emission line is ^{12}CO(4–3) at $z = 4.38$; however, ^{12}CO(5–4) would then be expected at 107.1 GHz, with a similar significance given the typical spectral-line energy distributions of DSFGs, and such a line is not detected (Fig. 7). ^{12}CO(3–2) and ^{12}CO(5–4) are the other most likely possibilities, at $z = 3.03$ and $z = 5.71$.

Towards NGP-111912 we detected a weak emission line at 95.15 GHz (Fig. 7), with an FWHM of 440 ± 200 km s^{-1}. The line emission is coincident spatially with 1.3-mm continuum emission (Fig. 2). With a photometric redshift estimate of $3.28^{+0.36}_{-0.26}$, the emission line may be ^{12}CO(4–3) at $z = 3.84$, in which case we would not expect any other lines in our current frequency coverage, consistent with our data.

SGP-32338 is a similar case: we detected an emission line at 101.07 GHz, with an FWHM of 630 ± 80 km s^{-1}. The line emission is again coincident with its 3-mm continuum emission (Fig. 2). The photometric redshift, $4.51^{+0.47}_{-0.39}$, makes ^{12}CO(5–4) at $z = 4.70$ the most likely candidate emission line. Because the line lies close to the centre of the spectral coverage, we would not then expect to detect any other lines, despite the high sensitivity and the wide frequency range available.

Follow-up observations are required to determine unambiguous redshifts for these three galaxies.

In SGP-354388, dubbed the 'Great Red Hope' because it is amongst the reddest galaxies seen by *Herschel*, our ALMA spectrum reveals a line at 98.34 GHz, coincident with 3-mm continuum emission. Extensive further follow-up observations of SGP-354388, reported by Oteo et al. (in preparation-b), confirm that the line at 98.34 GHz is, in fact, the C I(1–0) transition at $z = 4.002 \pm 0.001$, a rare $\approx 2\sigma$ deviation from the photometric redshift which can be attributed at least partially to dusty galaxies surrounding SGP-354388, at the same redshift, which contaminate the flux densities measured at ≥500 μm by SPIRE and LABOCA (Ivison et al. 2016).

[4] Gravitational lensing is found likely for three of the galaxies in this sample, as revealed by *K*-band imaging – see Fig. 4; the rest are devoid of close near-IR counterparts, though the depth of the available near-IR imaging does not exclude the possibility of distant ($z \gtrsim 1$) lenses.

[5] Due to its very high critical density, this line is very difficult to excite in emission, but it can be seen relatively easily in absorption, where there is strong background continuum. In the cold ISM, water is normally frozen out, forming icy mantles on dust grains; detecting this transition in absorption suggests water is gaseous, perhaps because of turbulence or shock heating.

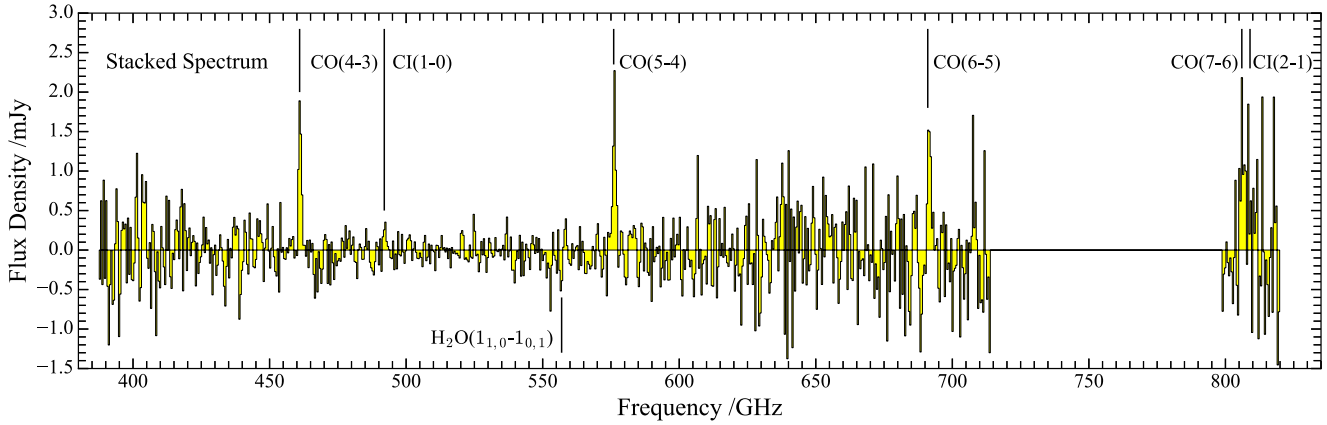

Figure 6. Rest-frame stacked spectrum, noise-weighted and continuum-subtracted, of the eight galaxies for which we have accurate, unambiguous redshifts, with lines marked, including the ^{12}CO ladder between $J = 4$–3 and $J = 7$–6, the latter broadened by C I(2–1), as well as weak C I(1–0) line emission. The position of H_2O $1_{1,0}$–$1_{0,1}$ is also marked, though the significance of the possible absorption line is only $\approx 2.5\sigma$.

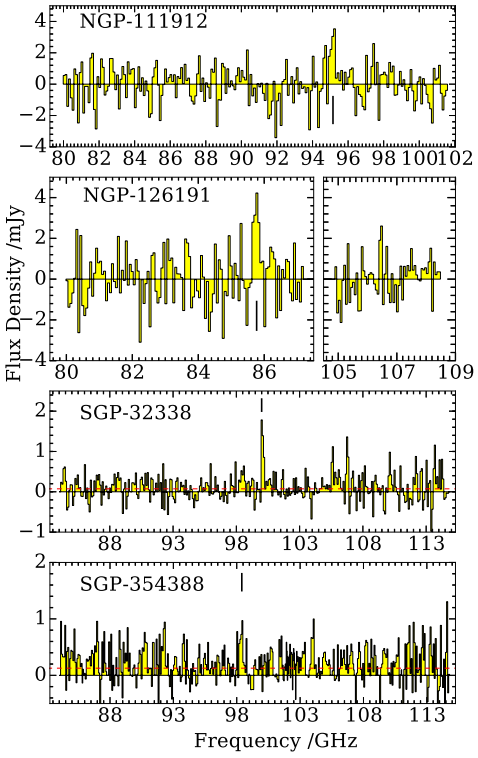

Figure 7. 3-mm spectra of NGP-111912, NGP-126191, SGP-32338 and SGP-354388, with channels binned to 350, 200, 200 and 350 km s^{-1}, respectively. The identification of the emission line and redshift are ambiguous for these sources, as no other emission line is detected convincingly. For NGP-111912, the spectrum has been extracted at the position of the 1.3-mm continuum; if we assume the emission line at 95.15 GHz is CO(4–3) at $z = 3.84$, where the photometric redshift estimate is $3.27^{+0.36}_{-0.26}$. For NGP-126191, the emission line seen at 85.77 GHz suggests $z = 4.38$, but the non-detection of another emission line near 107.1 GHz makes this unlikely. If we instead assume that NGP-126191 lies at $z = 5.71$, the emission line at 85.77 GHz becomes CO(5–4); $z \sim 3.03$ or $z \sim 7.06$ are also feasible. For SGP-32338 (where $z_{\rm ph} = 4.51^{+0.47}_{-0.39}$ Ivison et al. 2016), the emission line detected at 100.07 GHz could be CO(5–4) at $z = 4.70$. We would not then expect to detect other lines, despite the wide frequency coverage.

4.3.4 Galaxies where no emission lines are detected

In our remaining spectral scans, regardless of whether or not we have secure positions via continuum detections, we have found no compelling evidence of line emission (Fig. 8). Note that the mean [median] $\log_{10}$ far-IR luminosity of this subsample, 13.2 [13.1], for an average [median] photometric redshift of 3.79 [3.70], which is 0.3–0.4 dex below that of the sample in which line emission has been detected. For an FWHM line width of 500 km s^{-1} and typical brightness temperature and $L_{\rm IR}$/CO ratios (see later, Section 4.6), this equates to a peak line flux density in CO(4–3) of 1.6 [1.4] mJy, comparable to the r.m.s. noise levels in our spectral scans, which goes some considerable way towards explaining why we detected no line emission for this sub-sample.

4.4 Spectral energy distributions

Since we have added continuum flux density measurements at 1.3 and/or 3 mm for many of our targets, as well as some unambiguous spectroscopic redshifts, it is worth repeating the SED fits performed by Ivison et al. (2016). We have constructed the SEDs of our targets, utilizing data from SPIRE at 250, 350 and 500 μm, from SCUBA-2 at 850 μm (Ivison et al. 2016), from NOEMA at 1.3 mm and from NOEMA and/or ALMA at 3 mm – see Table 2. For details of the SED fits for SGP-32386, we refer readers to Oteo et al. (2016).

Like Ivison et al., we employ SED templates representative of high-redshift DSFGs: the average SEDs from Swinbank et al. (2014), Pope et al. (2008) and Pearson et al. (2013), and the observed SEDs of individual targets – the Cosmic Eyelash (Ivison et al. 2010b; Swinbank et al. 2010), HFLS 3 (Riechers et al. 2013), G15.141 (Cox et al. 2011) and Arp 220 (Donley et al. 2007).

We have restricted our SED work to the sources with unambiguous redshift determinations, such that we need shift only the flux density scale of the templates to fit the observed SEDs. We adopted the lowest χ^2 values, calculated from the difference between the templates and the observed flux densities, with inverse weighting of the flux density uncertainties. These best-fitting SEDs are plotted in Fig. 9, with the corresponding IR luminosities ($L_{8-1000\ \mu{\rm m}}$) and SFRs listed in Table 7, the latter calculated using the calibration of Hao et al. (2011), Murphy et al. (2011) and Kennicutt & Evans (2012), with a Salpeter IMF (although see Romano et al. 2017, for a cautionary tale regarding the IMF in such starbursts). On the basis

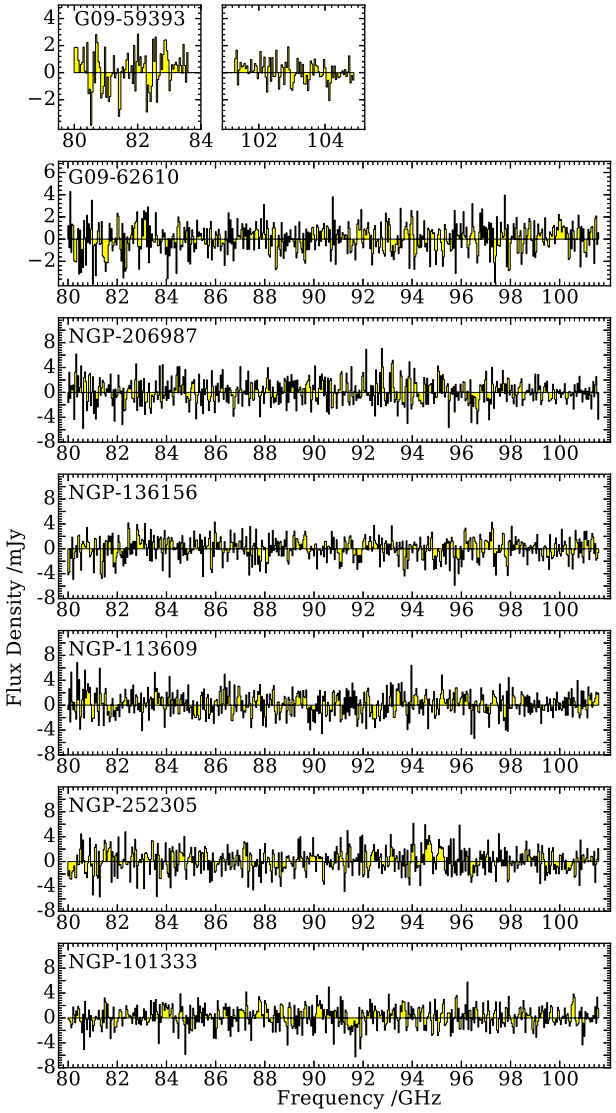

Figure 8. 3-mm spectra of G09-59393, G09-62619, NGP-206987, NGP-136156, NGP-113609 and NGP-252305, with channels binned to 200 km s^{-1}, all cases where we have secure positions via continuum detections at 1.3 and/or 3 mm, but where there is no strong evidence of line emission. The median $L_{\rm IR}$ for these galaxies, based on their photometric redshifts, is 0.3–0.4 dex below that of the galaxies with significant line emission, which goes some way towards explaining why we have detected no line emission in these cases.

of high-resolution ALMA continuum and line observations, Oteo et al. (2016) found that SGP-196076 at $z = 4.425$ comprises at least three components, their on-going merger driving large masses of turbulent gas to form stars, as is ubiquitous amongst objects with such high intrinsic IR luminosities (e.g. Frayer et al. 1998, 1999; Ivison et al. 1998, 2010a, 2013; Bothwell et al. 2013; Fu et al. 2013; Messias et al. 2014; Rawle et al. 2014; Dye et al. 2015; Geach et al. 2015; Thomson et al. 2015; Oteo et al. 2016).

4.4.1 Modified blackbody fits

To better quantify the thermal dust emission we have performed SED fits using modified blackbody (MBB) spectra, again by minimizing χ^2. We adopted an optically thin model with single dust temperature [i.e. $S_\nu(T_{\rm d}) \propto (\frac{\nu}{\nu_{\rm c}})^\beta\ B_\nu(T_{\rm d})$], where ν_c is the frequency

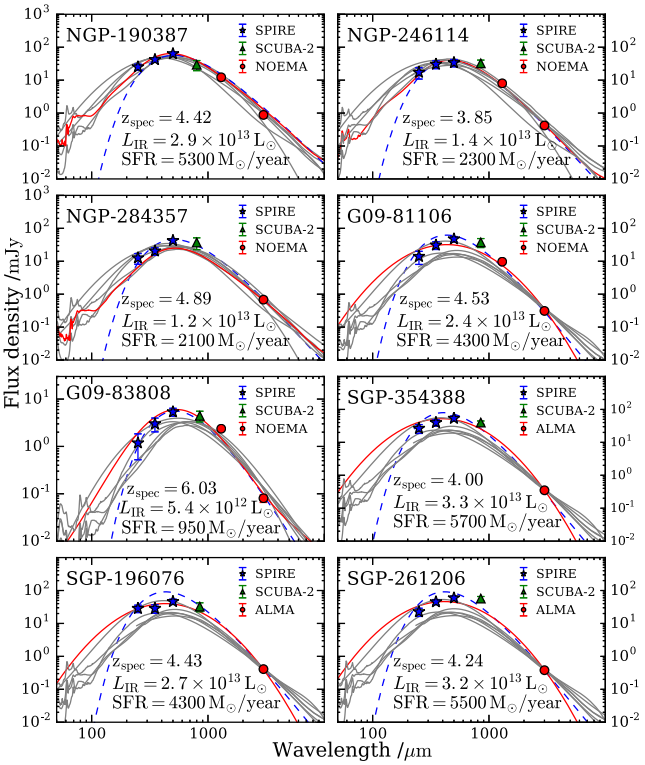

Figure 9. SEDs of those galaxies with unambiguous spectroscopic redshifts. Data are from *Herschel* SPIRE (blue; 250, 350 and 500 μm), SCUBA-2 (green; 850 μm) and NOEMA (red; 1.3 and/or 3 mm). Best-fitting SEDs are also shown – red solid lines for the best-fitting template, blue dashed lines for the best-fitting modified blackbody function, with other models scaled to minimize χ^2 shown as grey solid lines. Best-fitting templates: Pope et al. (2008) for NGP-190387; the Cosmic Eyelash (Swinbank et al. 2010; Ivison et al. 2010b) for NGP-246114 and NGP-284357; G15.141 (Cox et al. 2011) for G09-81106, SGP-354388, SGP-196076 and SGP-261206. IR luminosities are calculated using the best-fitting template between rest frame 8 and 1000 μm, and SFR is estimated using these IR luminosities with a Salpeter IMF and the empirical calibration of Hao et al. (2011), Murphy et al. (2011) and Kennicutt & Evans (2012). The values displayed have not been corrected for gravitational amplification, μ (see Table 7 for μ-corrected values). Dust temperatures and masses determined from the modified blackbody fits are listed in Table 6.

at which the optical depth is unity, $B_\nu(T_{\rm d})$ is Planck function at frequency, ν, and dust temperature, $T_{\rm d}$, and β is the dust emissivity index. We fixed $\nu_{\rm c}$ to 1.5 THz (e.g. Conley et al. 2011; Rangwala et al. 2011) and adopted $\kappa_{850\ \mu{\rm m}} = 0.15$ m^2 kg^{-1} (Weingartner & Draine 2001; Dunne, Eales & Edmunds 2003). Dust emissivity, β, being poorly constrained by our data, was fixed to values of 1.5, 2.0 or 2.5 (Dunne & Eales 2001; Casey et al. 2011; Chapin et al. 2011; Magnelli et al. 2012; Walter et al. 2012).

The assumption of a single dust temperature means that we are measuring the emission-weighted mean dust temperature and dust mass of all the dust components in the galaxy. Another advantage of this approach is that it allows us to compare directly with other high-redshift DSFGs, which are usually described in terms of single-temperature MBB fits (see Table 7). Finally, the modest sampling of our SEDs, especially at the short wavelengths required to constrain hot dust components, prevents meaningful multi-temperature MBB fitting.

The best MBB fits are plotted in Fig. 9. Minimum χ^2 were obtained with $\beta = 1.5$ for NGP-190387, $\beta = 2.0$ for NGP-246114

Table 6. Dust temperatures and masses.

Object	T_d/(K)	M_d/($M_\odot$)	β
SGP-196076[a]	∼33	$\sim 2.6 \times 10^9$	2.0
SGP-261206[b]	33.1 ± 0.5	–	2.5
SGP-354388	32.3 ± 0.8	$1.4 \pm 0.2 \times 10^9$	2.5
G09-81106	34.7 ± 1.0	$8.6 \pm 1.0 \times 10^8$	2.5
G09-83808[c]	35.9 ± 1.5	$2.1 \pm 0.3 \times 10^8$	2.5
NGP-284357	33.3 ± 1.4	$2.3 \pm 0.4 \times 10^9$	2.0
NGP-190387[b]	34.4 ± 1.1	–	1.5
NGP-246114	30.7 ± 1.1	$2.0 \pm 0.3 \times 10^9$	2.0

[a]From table 2 of Oteo et al. (2016): T_d is average of brightest two components; dust mass is their sum.
[b]SGP-261206 and NGP-190387 are gravitationally lensed; only T_d is constrained as the magnification factors are unknown.
[c]G09-83808 is gravitationally amplified by a factor 8.2 ± 0.3 (Oteo et al., in preparation-a).

and NGP-284357. G09-81106 proved difficult to reconcile with a value of β below 2.5 – probably the result of using a single temperature MBB (see e.g. Walter et al. 2012). Changing β results in an increase/decrease of the dust temperature by ∼2–3 K, and the dust mass by ∼0.1 dex. The resulting dust temperatures are in the range ∼31–36 K, and dust masses, ~ 0.2–$4.1 \times 10^9\,M_\odot$. For their high IR luminosities, the dust temperatures of our galaxies are relatively low (see e.g. Symeonidis et al. 2013). Individual values of T_d and M_d are listed in Table 6.

4.5 Molecular gas masses

Although low-J transitions of CO, or C I, are much preferred when tracing the remaining reservoirs of molecular hydrogen (Ivison et al. 2011; Papadopoulos et al. 2012), we can estimate those gas masses from higher J CO lines by assuming the average CO line ratio for SMGs, as measured by Greve et al. (2005), Tacconi et al. (2006), Tacconi et al. (2008), Ivison et al. (2011), Riechers et al. (2011) and Bothwell et al. (2013), and tabulated by the latter: $L'_{CO(7-6)}/L'_{CO(1-0)} = 0.18$, $L'_{CO(6-5)}/L'_{CO(1-0)} = 0.21$, $L'_{CO(5-4)}/L'_{CO(1-0)} = 0.32$ and $L'_{CO(4-3)}/L'_{CO(1-0)} = 0.41$, bearing in mind that there can be large variations. We find that $L_{IR} - L'_{CO}$ as derived from different – usually neighbouring – transitions are consistent. We have taken the average $L'_{CO(1-0)}$ from the available high-J CO transitions, then calculated the molecular gas masses using $\alpha_{CO} = 0.8\,M_\odot\,(K\,km\,s^{-1}\,pc^2)^{-1}$, the value often assumed for high-redshift starbursts and local ULIRGs since the work of Downes & Solomon (1998). Estimates of gas-to-dust mass ratios then lie in the range 50–140, consistent with those of local galaxies. Our M_{H_2} estimates are listed in Table 7.

Since luminous CO(5–4) and CO(4–3) emission can be generated by the presence of a massive molecular gas reservoir, or by a much smaller amount of highly excited molecular gas, follow-up observations of low-J CO transitions are required to better determine M_{H_2}, modulo the effects of cosmic rays laid out by Bisbas et al. (2017).

4.6 L_{IR}–L'_{CO} correlation

The relationship between star formation and total molecular gas content is often shown via a plot of the key observables, L_{IR} versus L'_{CO}, and can reveal if and how star-formation efficiency (SFE) changes with the amount of molecular gas available for star formation. We have constructed a plot of L_{IR}–L'_{CO} using our $z > 4$ IR-luminous galaxies, other high-redshift unlensed DSFGs (Ivison et al. 2011; Bothwell et al. 2013; Greve et al. 2014) and local U/LIRGS (Papadopoulos et al. 2012) – see Fig. 10. A linear fit to all the data has a slope, 1.15 ± 0.02 (see also, e.g. Iono et al. 2009; Genzel et al. 2010; Ivison et al. 2011; Bothwell et al. 2013).

Caution is required here, however, since most of the high-redshift targets, ours included, are detected in mid-J CO transitions. Using only CO(1–0) observations, with self-consistent determinations of IR luminosity, Ivison et al. (2011) reported a slope significantly below unity, showing that adopting mid-J CO transitions for high-redshift galaxies and CO(1–0) transitions for low-redshift galaxies may artificially steepen the slope. Differential amplification is likely

Table 7. Properties compared to other $z \gtrsim 4$ galaxies.

Name	Redshift	SFR[a] ($M_\odot\,yr^{-1}$)	$M^b_{H_2}$ ($10^{11}\,M_\odot$)	L_{IR} ($10^{13}\,L_\odot$)	Known to be lensed?	Reference
SGP-261206	4.242	$5500/\mu$	$3.2/\mu$	$1.3/\mu$	Yes[c]	This work
G09-81106	4.531	4300	1.2	2.4	No	This work
NGP-284357	4.894	2100	2.1	1.2	No	This work
NGP-190387	4.420	$5300/\mu$	$2.1/\mu$	$2.9/\mu$	Yes[c]	This work
NGP-246114	3.847	2300	0.99	1.4	No	This work
HFLS 1	4.29	9700	–	5.6	No	Dowell et al. (2014)
G09-83808	6.027	$7800/\mu$	$0.78/\mu$	$4.4/\mu$	Yes[c]	Zavala et al. (2017)
ADFS-27	5.655	4200	2.5	2.5	No	Riechers et al. (2017)
SGP-354388	4.002	5700	–	3.3	No	Oteo et al. (in preparation-b)
SGP-196076	4.425	4300[d]	2.7	2.4	No	Oteo et al. (2016)
GN 20	4.055	3000	1.3	2.9	No	Hodge et al. (2012)
HDF 850.1	5.183	$850/\mu$	0.35	0.65	Weakly[c]	Walter et al. (2012)
AzTEC-1	4.342	2000	$1.4/\mu$	$1.4/\mu$	No	Yun et al. (2015)
AzTEC-3	5.299	1800	0.53	1.1	No	Riechers et al. (2014)
HFLS 3	6.337	$2100/\mu$	$0.36/\mu$	$2.9/\mu$	Weakly[c]	Riechers et al. (2013)

[a]SFRs derived from L_{IR} (rest frame 8–1000 μm), and empirical calibration by Hao et al. (2011); Murphy et al. (2011); Kennicutt & Evans (2012), i.e. SFR = $L_{IR}/2.21 \times 10^{43}\,M_\odot\,yr^{-1}$, adjusting to a Salpeter IMF.
[b]Molecular gas masses, assuming $\alpha_{CO} = M_{gas}/L'_{CO} = 0.8\,M_\odot/(K\,km\,s^{-1}\,pc^2)$, typical for high-redshift starbursts and a small sample of local ULIRGs (Downes & Solomon 1998).
[c]For lensed galaxies, listed values are uncorrected for the magnification, μ.
[d]Total SFR of the most luminous two components (Oteo et al. 2016).

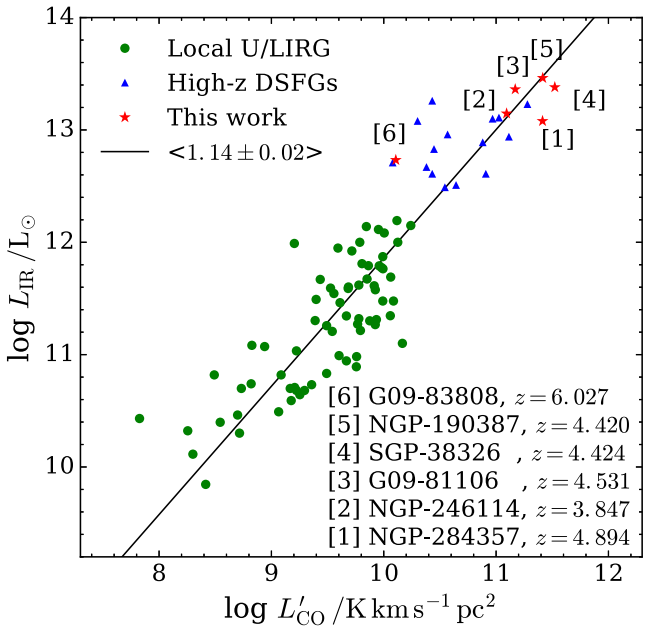

Figure 10. $L_{\rm IR}$–$L'_{\rm CO}$ correlation of local U/LIRGs and high-redshift DSFGs. Green circles: CO(1–0) observations of local U/LIRGs (Papadopoulos et al. 2012); blue triangles: high-redshift DSFGs with CO(1–0) observations (Ivison et al. 2011) and with mid-J CO observations (Bothwell et al. 2013; Greve et al. 2014). For SGP-196076, we used the sum of the two most luminous components of the merging system. Mid-J transitions have been converted to CO(1–0) line luminosities using line luminosity ratio tabulated by Bothwell et al. (2013). Black solid line: linear fit to all data points (i.e. $\log L_{\rm IR} = \alpha\ \log L'_{\rm CO} + \beta$, where α and β are free parameters). The resulting slope, $\alpha = 1.14 \pm 0.02$.

also an issue for the lensed galaxies in Fig. 10, where the amplifications derived for the dust, the CO(1–0) and/or high-J CO lines likely differ significantly. Finally, we note that several studies have suggested that our adopted value of $\alpha_{\rm CO}$ is too low, including Weiß et al. (2007) and Papadopoulos et al. (2012); indeed, if we were to apply the formalism of Scoville et al. (2016), who use optically thin long-wavelength dust emission to probe the mass of molecular gas, we arrive at a value $\sim$3.5 $\times$ higher, the equivalent of $\alpha_{\rm CO} \approx 3\,{\rm M}_\odot\,({\rm K\,km\,s^{-1}\,pc^2})^{-1}$.

4.7 Depletion time-scale

The average gas-depletion time-scale of our galaxies, $t_{\rm depl}$, is around 50 Myr, modulo the possibility of considerably higher gas masses noted in Section 4.6. Taken at face value, this $t_{\rm depl}$ is consistent with the idea that our targets are rapidly building a significant mass of stars, which may be picked up in a later phase at $z \sim$ 2–3 as massive 'red-and-dead' galaxies by near-IR imaging surveys (e.g. Cimatti et al. 2004; Trujillo et al. 2006; van Dokkum & Brammer 2010).

5 CONCLUSIONS

We report spectral scans of *Herschel*-selected ultra-red galaxies with photometric redshifts estimated to lie at $\gtrsim$4. For each of 21 galaxies, we have covered $\Delta\nu \approx$20 GHz using ALMA and NOEMA in the 3-mm waveband. We have determined the redshifts of seven galaxies unambiguously, in the range $z = 3.85$–6.03, detecting multiple emission lines, usually CO rotational transitions. One of these redshifts was determined independently by Zavala et al. (2017).

For an additional four galaxies, single emission lines are detected, one of which has been shown by Oteo et al. (in preparation-b) to lie at $z = 4.002$. Candidate redshifts are suggested, based on their photometric redshifts. Follow-up observations are required to measure their redshifts unambiguously, except in that one case.

Since the comparison of photometric and spectroscopic redshifts for this sample by Ivison et al. (2016), two new spectroscopic redshifts have been determined, one below and one above the respective photometric redshifts. Although the offsets for these two galaxies are larger than the expected uncertainties in $z_{\rm phot}$, the overall scatter in $(z_{\rm phot} - z_{\rm spec})/(1 + z_{\rm spec})$ is still consistent with (actually, slightly better than) that of the training set. In the worst case, the offset can be understood in terms of contamination of flux densities measured at $\geq$500 μm by a cluster of dusty galaxies (Oteo et al., in preparation-a).

Our sample of redshift-confirmed galaxies contains extraordinarily IR-luminous starbursts, with an average SFR of $\approx$2900 ${\rm M}_\odot\ {\rm yr}^{-1}$. They are also amongst the most massive known, in terms of molecular gas mass, and dust mass, with $M_{\rm H_2} \approx 1.8 \times 10^{11}\ {\rm M}_\odot$ on average, and $M_{\rm d} \sim 0.9$–$4.1 \times 10^9\ {\rm M}_\odot$.

Lurking amongst our IR-luminous galaxies, we find three lensed systems. These would otherwise have been hailed as the most luminous known starbursts. It is notable that the vast majority of the brightest systems selected by *Herschel* have been revealed as either lensed galaxies, groups/clusters of starburst galaxies, starbursts with buried active galactic nuclei, or some combination of the three (e.g. Ivison et al. 2013; Oteo et al. 2016), which suggests strongly that there exists a limit to the luminosity of individual starbursting galaxies.

Combining local U/LIRGs, other high-redshifts DSFGs and our new redshift-confirmed galaxies, the resulting $L_{\rm IR}$–$L'_{\rm CO}$ correlation has slope close to unity, 1.14 ± 0.02, suggesting slightly higher SFE in the most IR-bright galaxies.

The gas-depletion time-scale of our galaxies, around 50 Myr, is consistent with the idea that our targets may be picked up in a later phase at $z \sim$ 2–3 as massive 'red-and-dead' galaxies by near-IR imaging surveys.

ACKNOWLEDGEMENTS

RJI, IO, VA, LD, SM, JMS and ZYZ acknowledge support from the European Research Council in the form of the Advanced Investigator Programme, 321302, COSMICISM. JMS also acknowledges financial support through an EACOA fellowship. DR acknowledges support from the National Science Foundation under grant number AST-1614213. HD acknowledges financial support from the Spanish Ministry of Economy and Competitiveness (MINECO) under the 2014 Ramón y Cajal program, MINECO RYC-2014-15686. We thank the referee, Francoise Combes, for her rapid and constructive feedback. This work was based on observations carried out with the IRAM Interferometer, NOEMA, supported by INSU/CNRS (France), MPG (Germany), and IGN (Spain). This paper makes use of the following ALMA data: ADS/JAO.ALMA#2013.1.00499.S. ALMA is a partnership of ESO (representing its member states), NSF (USA) and NINS (Japan), together with NRC (Canada) and NSC and ASIAA (Taiwan) and KASI (Republic of Korea), in cooperation with the Republic of Chile. The Joint ALMA Observatory is operated by ESO, AUI/NRAO and NAOJ. Based on observations collected at the European Organisation for Astronomical Research in the Southern Hemisphere under ESO programme 090.A-0891(A). Based on observations obtained at the Gemini Observatory, which is operated by the Association of Universities for

Research in Astronomy, Inc., under a cooperative agreement with the NSF on behalf of the Gemini partnership: the National Science Foundation (United States), the National Research Council (Canada), CONICYT (Chile), Ministerio de Ciencia, Tecnología e Innovación Productiva (Argentina) and Ministério da Ciência, Tecnologia e Inovação (Brazil).

REFERENCES

Asboth V. et al., 2016, MNRAS, 462, 1989
Barger A. J., Cowie L. L., Sanders D. B., Fulton E., Taniguchi Y., Sato Y., Kawara K., Okuda H., 1998, Nature, 394, 248
Bethermin M. et al., 2017, preprint (arXiv:1703.08795)
Bisbas T. G., van Dishoeck E. F., Papadopoulos P. P., Szűcs L., Bialy S., Zhang Z.-Y., 2017, ApJ, 839, 90
Bothwell M. S. et al., 2013, MNRAS, 429, 3047
Bruzual G., Charlot S., 2003, MNRAS, 344, 1000
Casey C. M. et al., 2011, MNRAS, 415, 2723
Casey C. M., Narayanan D., Cooray A., 2014, Phys. Rep., 541, 45
Chapin E. L. et al., 2011, MNRAS, 411, 505
Chapman S. C., Blain A. W., Smail I., Ivison R. J., 2005, ApJ, 622, 772
Christensen L. et al., 2012, MNRAS, 427, 1953
Cimatti A. et al., 2004, Nature, 430, 184
Combes F. et al., 2012, A&A, 538, L4
Conley A. et al., 2011, ApJ, 732, L35
Cox P. et al., 2011, ApJ, 740, 63
da Cunha E. et al., 2015, ApJ, 806, 110
Donley J. L., Rieke G. H., Pérez-González P. G., Rigby J. R., Alonso-Herrero A., 2007, ApJ, 660, 167
Dowell C. D. et al., 2014, ApJ, 780, 75
Downes D., Solomon P. M., 1998, ApJ, 507, 615
Dunlop J., Peacock J., Spinrad H., Dey A., Jimenez R., Stern D., Windhorst R., 1996, Nature, 381, 581
Dunne L., Eales S. A., 2001, MNRAS, 327, 697
Dunne L., Eales S. A., Edmunds M. G., 2003, MNRAS, 341, 589
Dye S. et al., 2015, MNRAS, 452, 2258
Eales S., Lilly S., Gear W., Dunne L., Bond J. R., Hammer F., Le Fèvre O., Crampton D., 1999, ApJ, 515, 518
Eales S. et al., 2010, PASP, 122, 499
Eales S., de Vis P. W. L. Smith M., Appah K., Ciesla L., Duffield C., Schofield S., 2017, MNRAS, 465, 3125
Edge A., Sutherland W., Kuijken K., Driver S., McMahon R., Eales S., Emerson J. P., 2013, The Messenger, 154, 32
Frayer D. T., Ivison R. J., Scoville N. Z., Yun M., Evans A. S., Smail I., Blain A. W., Kneib J.-P., 1998, ApJ, 506, L7
Frayer D. T. et al., 1999, ApJ, 514, L13
Fu H. et al., 2013, Nature, 498, 338
Geach J. E. et al., 2015, MNRAS, 452, 502
Genzel R. et al., 2010, MNRAS, 407, 2091
Greve T. R. et al., 2005, MNRAS, 359, 1165
Greve T. R. et al., 2014, ApJ, 794, 142
Griffin M. J. et al., 2010, A&A, 518, L3+
Hao C.-N., Kennicutt R. C., Johnson B. D., Calzetti D., Dale D. A., Moustakas J., 2011, ApJ, 741, 124
Hodge J. A., Carilli C. L., Walter F., de Blok W. J. G., Riechers D., Daddi E., Lentati L., 2012, ApJ, 760, 11
Holland W. S. et al., 2013, MNRAS, 430, 2513
Hughes D. H. et al., 1998, Nature, 394, 241
Iono D. et al., 2009, ApJ, 695, 1537
Ivison R. J., Smail I., Le Borgne J.-F., Blain A. W., Kneib J.-P., Bezecourt J., Kerr T. H., Davies J. K., 1998, MNRAS, 298, 583
Ivison R. J., Smail I., Papadopoulos P. P., Wold I., Richard J., Swinbank A. M., Kneib J.-P., Owen F. N., 2010a, MNRAS, 404, 198
Ivison R. J. et al., 2010b, A&A, 518, L35
Ivison R. J., Papadopoulos P. P., Smail I., Greve T. R., Thomson A. P., Xilouris E. M., Chapman S. C., 2011, MNRAS, 412, 1913
Ivison R. J. et al., 2013, ApJ, 772, 137
Ivison R. J. et al., 2016, ApJ, 832, 78
Kausch W. et al., 2014, in Manset N., Forshay P., eds, ASP Conf. Ser. Vol. 485, Astronomical Data Analysis Software and Systems XXIII. Astron. Soc. Pac., San Francisco, p. 403
Kennicutt R. C., Evans N. J., 2012, ARA&A, 50, 531
Kriek M., van der Wel A., van Dokkum P. G., Franx M., Illingworth G. D., 2008, ApJ, 682, 896
Magnelli B. et al., 2012, A&A, 539, A155
McMullin J. P., Waters B., Schiebel D., Young W., Golap K., 2007, in Shaw R. A., Hill F., Bell D. J., eds, ASP Conf. Ser. Vol. 376, Astronomical Data Analysis Software and Systems XVI. Astron. Soc. Pac., San Francisco, p. 127
Messias H. et al., 2014, A&A, 568, A92
Modigliani A. et al., 2010, in Silva D. R., Peck A. B., Soifer B. T., Proc. SPIE Conf. Ser. Vol. 7737, Observatory Operations: Strategies, Processes, and Systems III. SPIE, Bellingham, p. 773728
Murphy E. J. et al., 2011, ApJ, 737, 67
Negrello M. et al., 2010, Science, 330, 800
Oteo I. et al., 2016, ApJ, 827, 34
Papadopoulos P. P., van der Werf P. P., Xilouris E. M., Isaak K. G., Gao Y., Mühle S., 2012, MNRAS, 426, 2601
Pearson E. A. et al., 2013, MNRAS, 435, 2753
Pilbratt G. L. et al., 2010, A&A, 518, L1
Pope A. et al., 2008, ApJ, 689, 127
Puget J.-L., Abergel A., Bernard J.-P., Boulanger F., Burton W. B., Desert F.-X., Hartmann D., 1996, A&A, 308, L5
Rangwala N. et al., 2011, ApJ, 743, 94
Rawle T. D. et al., 2014, ApJ, 783, 59
Renzini A., 2006, ARA&A, 44, 141
Riechers D. A. et al., 2011, ApJ, 733, L11
Riechers D. A. et al., 2013, Nature, 496, 329
Riechers D. A. et al., 2014, ApJ, 796, 84
Riechers D. A. et al., 2017, preprint (arXiv:1705.09660)
Romano D., Matteucci F., Zhang Z.-Y., Papadopoulos P. P., Ivison R. J., 2017, MNRAS, 470, 401
Scoville N. et al., 2016, ApJ, 820, 83
Simpson J. M. et al., 2014, ApJ, 788, 125
Siringo G. et al., 2009, A&A, 497, 945
Smail I., Ivison R. J., Blain A. W., 1997, ApJ, 490, L5
Soifer B. T., Neugebauer G., Houck J. R., 1987, ARA&A, 25, 187
Spilker J. S. et al., 2015, ApJ, 811, 124
Strandet M. L. et al., 2017, ApJ, 842, L15
Swinbank A. M. et al., 2010, Nature, 464, 733
Swinbank A. M. et al., 2014, MNRAS, 438, 1267
Symeonidis M. et al., 2013, MNRAS, 431, 2317
Tacconi L. J. et al., 2006, ApJ, 640, 228
Tacconi L. J. et al., 2008, ApJ, 680, 246
Thomas D., Maraston C., Schawinski K., Sarzi M., Silk J., 2010, MNRAS, 404, 1775
Thomson A. P., Ivison R. J., Owen F. N., Danielson A. L. R., Swinbank A. M., Smail I., 2015, MNRAS, 448, 1874
Toft S. et al., 2014, ApJ, 782, 68
Trujillo I. et al., 2006, MNRAS, 373, L36
Valiante E. et al., 2016, MNRAS, 462, 3146
van Dokkum P. G., Brammer G., 2010, ApJ, 718, L73
Vieira J. D. et al., 2010, ApJ, 719, 763
Walter F. et al., 2012, Nature, 486, 233
Weingartner J. C., Draine B. T., 2001, ApJ, 548, 296
Weiß A., Downes D., Neri R., Walter F., Henkel C., Wilner D. J., Wagg J., Wiklind T., 2007, A&A, 467, 955
Weiß A., Ivison R. J., Downes D., Walter F., Cirasuolo M., Menten K. M., 2009, ApJ, 705, L45
Weiß A. et al., 2013, ApJ, 767, 88
Yun M. S. et al., 2015, MNRAS, 454, 3485
Zavala J. A. et al., 2017, Nat. Astron., preprint (arXiv:1707.09022)
Zhang Z.-Y. et al., 2017, MNRAS, submitted

[1]*Observatoire de Genève, 51 Ch. des Maillettes, CH-1290 Versoix, Switzerland*
[2]*ESO, Karl-Schwarzschild-Str 2, D-85748 Garching, Germany*
[3]*Institute for Astronomy, University of Edinburgh, Royal Observatory, Blackford Hill, Edinburgh EH9 3HJ, UK*
[4]*Institut de RadioAstronomie Millimétrique, 300 rue de la Piscine, Domaine Universitaire, F-38406 Saint Martin d'Hères, France*
[5]*Max-Planck-Institut für Radioastronomie, Auf dem Hügel 69, D-53121 Bonn, Germany*
[6]*IAC, E-38200 La Laguna, Tenerife, Spain*
[7]*Departamento de Astrofisica, Universidad de La Laguna, E-38205 La Laguna, Tenerife, Spain*
[8]*UPMC Univ Paris 06, UMR 7095, IAP, F-75014 Paris, France*
[9]*CNRS, UMR7095, IAP, F-75014 Paris, France*
[10]*Department of Physics and Atmospheric Science, Dalhousie University, Halifax NS B3H 4R2, Canada*
[11]*Dark Cosmology Centre, Niels Bohr Institute, University of Copenhagen, Juliane Maries Vej 30, DK-2100 Copenhagen, Denmark*
[12]*Argelander-Institute for Astronomy, Bonn University, Auf dem Huegel 71, D-53121 Bonn, Germany*
[13]*H. H. Wills Physics Laboratory, University of Bristol, Tyndall Avenue, Bristol BS8 1TL, UK*
[14]*Astrophysics Group, Imperial College London, Blackett Laboratory, Prince Consort Road, London SW7 2AZ, UK*
[15]*School of Physics & Astronomy, Cardiff University, Queen's Buildings, The Parade, Cardiff CF24 3AA, UK*
[16]*Astronomy Department, Cornell University, Ithaca, NY 14853, USA*
[17]*Academia Sinica Institute of Astronomy and Astrophysics, No. 1, Section 4, Roosevelt Rd, Taipei 10617, Taiwan*
[18]*Institute for Astronomy, University of Hawaii, 2680 Woodlawn Drive, Honolulu, HI 96822, USA*
[19]*Leiden Observatory, Leiden University, P.O. Box 9513, NL-2300 RA Leiden, the Netherlands*

This paper has been typeset from a TEX/LATEX file prepared by the author.